Convex Optimization of Wideband Monopulse Arrays

Henrik Frid, Harald Hultin, and B. L. G. Jonsson

Abstract— A convex optimization program is presented for wideband arrays. Constraints are imposed on the frequency variation of excitation coefficients to ensure that the optimal solution can be realized in a wideband active electronically scanned array (AESA). AESA implementation with true time delays (TTDs) and phase shifters are handled separately. We also discuss the general case of combining TTDs and phase shifters. Contrary to single-frequency optimization, the wideband optimization method presented here ensures that the computed excitation is optimal over a specified bandwidth. It is shown that there is a tradeoff between instantaneous bandwidth and sidelobe level. The proposed method works for both narrow and wideband arrays, as illustrated with examples. In addition to regular arrays, the method is also applicable to monopulse arrays. The optimization program is implemented in terms of embedded element patterns (EEPs) to account for and compensate for mutual coupling, radome, and platform effects.

Index Terms— Arrays, direction-of-arrival (DoA) estimation, electronic warfare (EW), optimization methods.

I. INTRODUCTION

THE bandwidths of array antenna products vary significantly depending on the application. The bandwidths found in electronic warfare (EW) systems are typically significantly larger than those used for radar and communications. The demand for extremely large bandwidths in EW systems comes from the need to detect multiple emitters without knowing their operation frequencies beforehand [1]. Electronic support measures (ESMs) systems, therefore, typically use wideband active electronically scanned arrays (AESAs) to cover several radar frequency bands. An important task for an ESM system is direction-of-arrival (DoA) estimation. In this article, we will first focus on a four-quadrant monopulse array with common excitation weights used for DoA estimation, as described in, for example, [2], [3], [4]. While EW systems have a significantly larger bandwidth than radar or

communication systems, our method works for arrays with any bandwidth. We also demonstrate that the presented method is useful in narrowband arrays used for communications applications. Improvements beyond single-frequency optimization are demonstrated.

There are multiple reasons for optimizing AESAs for low sidelobe levels. Considering airborne EW, this first reduces the sensitivity to interference and ground or sea clutter outside the mainlobe. Furthermore, a monopulse array requires a guard function used to determine whether a specific signal was received in the sidelobes or the mainlobe [2]. A lower sidelobe level will make the implementation of the guard function less challenging, and this is an additional reason for striving for optimally low sidelobes. Considering radar, lower sidelobe levels reduce the risk of being detected by an enemy surveillance system positioned outside the mainlobe.

There are numerous methods for determining optimal excitation weights for array antennas. Most optimization methods for array antennas are developed for a single frequency, for example, [4], [5], [6], [7], [8], [9], [10], [11]. One method of applying a single-frequency optimization method to a frequency band is to apply the optimization at the center frequency, with reduced performance in the edges of the frequency band as a result. This approach may be sufficient for narrowband communication and radar systems. Due to the reduced performance at the band edges, such methods are not suitable for EW AESAs. Another alternative method is to carry out single-frequency optimization at each frequency sample within the bandwidth. This approach has been investigated for endfire arrays, where it was shown to result in a rapidly fluctuating phase across the frequency band [12]. Without additional constraints on the frequency variation of the amplitude and phase coefficients, the optimal excitation obtained with single-frequency methods could, therefore, be difficult to realize in a practical system.

Fig. 1(a) shows an illustration of an AESA in the *receiving* mode. In an AESA, each antenna element is connected to a transmit/receive module (TRM) with both phase control and an amplifier unit. We will focus on the monopulse configuration in the receive mode. Due to the reciprocity of the array pattern, the convex optimization program presented here is also applicable to the transmit (Tx) mode. The phase control is applied using phase shifters and/or TTDs. Ideally, phase shifters produce a phase shift which is independent of frequency within the bandwidth, while TTDs produce a phase shift which is proportional to the frequency. Similarly,
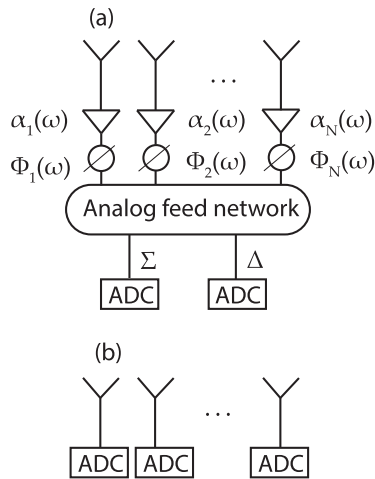
Fig. 1. (a) Illustration of an AESA with N elements in the receiving (Rx) mode. Each antenna element has a frequency-dependent gain coefficient $\alpha_n(\omega)$ and a frequency-dependent phase coefficient $\Phi_n(\omega)$. The phase coefficients can be applied using phase shifters, true time delays (TTDs), or a combination of both. The feed network forms the sum and differences of the signals from the corresponding subarrays. In this figure, two channels (Σ and Δ) are received by two analog-to-digital converters (ADCs), although it is possible to have more channels, in general. (b) Illustration of a digital Rx array, where each antenna element is connected to an individual ADC.
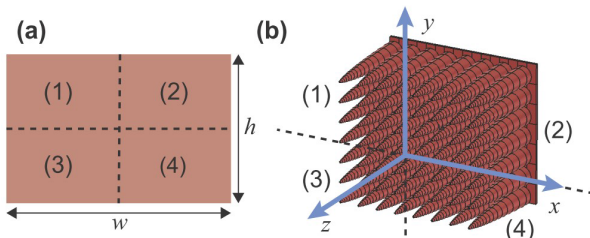

Fig. 2. (a) Illustration of the four-quadrant monopulse array configuration. (b) BoR array in the four-quadrant monopulse configuration.

a variable-gain amplifier (VGA) can be designed for a gain that is ideally independent of frequency within the bandwidth, or to vary linearly with a specified gain slope. The measured relation between gain and frequency together with nonlinearities for a state-of-the-art VGA design is presented in, for example, [13]. For the optimal excitation to be realizable in a wideband AESA implemented with VGAs and TTDs, there is, therefore, a need to introduce constraints that make each frequency sample dependent on the adjacent frequency samples. This is here referred to as wideband array optimization, as opposed to the single-frequency optimization described above.

While the TRM can be modeled as a linear device, it will have nonlinear characteristics that depend on the power level. Nonlinearities in the amplifier of the TRM can give rise to such effects as reduced gain in the mainlobe or sidelobes at intermodulated frequencies [14]. As we focus on a monopulse configuration in receive mode, we assume that the signals are weak and the TRMs operate in the linear region. Therefore, the modeling of nonlinearities in array antennas is beyond the scope of this article.

It is interesting to note that the situation for digital array antennas, as illustrated in Fig. 1(b), is somewhat different compared to an analog array antenna Fig. 1(a). In a digital array antenna, the amplitude and phase coefficients are applied

digitally. For purely digital signals, the frequency variation of the applied coefficient is of less concern and will not be treated in this article. There are a number of good references on the general topic of wideband beamforming, for example, [15], [16], [17]. Frequency-invariant beamforming has also been achieved using convex subproblems [18]. The method presented in this article instead formulates the whole beamforming problem as one convex problem. Furthermore, the broadband convex method of [19] has been compared to a Fourier transform-based method in [20]. Compared to the method presented in this article, [19] uses a finite impulse response beamformer with more degrees of freedom than the TRM used here. The largest bandwidth presented in [19] is 1:2, compared to the 1:5 bandwidth presented in Section IV of this article.

The convex optimization program presented in this article can be used for three TRM implementations, here referred to as Case A, Case B, and Case C, respectively. Case A assumes that a combination of phase shifters and TTDs are used in each TRM. Case B assumes that only TTDs but not phase shifters are used, whereas Case C assumes that phase shifters but not TTDs are used.

The article is organized as follows. First, Section II-A introduces the notation that will be used in the remainder of the article. Thereafter, Sections II-B and II-C present the constraints on the frequency variation of the amplitude and phase coefficients for wideband optimization. Section III-A presents a convex optimization program for optimal wideband sum patterns with low sidelobes for Cases A and C. The optimization program is modified for Case B in Section III-B. Section III-C presents a convex optimization program for optimal wideband difference patterns with low sidelobes. Section III-D presents a convex optimization program used for common excitation weights, that is, to find the tradeoff that results in simultaneously low sidelobes in sum and difference patterns that share common excitation weights. Numerical results are presented in Section IV. We do not present simulation results for Case C for the sake of brevity. We are mainly interested in very wideband EW AESAs where the beam squint inherent in using phase shifters is not acceptable. Furthermore, the TRM configuration of Case C is compatible with the program for Case A for which we present results. Finally, conclusions are presented in Section V.

II. BACKGROUND THEORY

A. Array Pattern as a Sum of EEPs

By formulating the optimization algorithm in terms of embedded element patterns (EEPs), the effects of mutual coupling can be taken into account in the optimization [7], [12]. The advantages of using EEPs in the optimization are particularly clear for aperiodic arrays [7] and small-array antennas [4]. For an array of N elements, the EEPs can be determined from N simulations or measurements, where one element is excited at a time while the remaining elements are terminated in matched loads [21]. For each EEP simulation, the total radiated field is stored together with the complex power received at each port. Using the power

received at element m (b_m) when the exciting element n with the excitation coefficient a_n, the coupling can be found via the scattering matrix $b = Sa$. Coupled power also causes nonexcited elements to radiate, which is included in the EEP.

By including the installation configuration in these simulations, the installed EEPs (IEEPs) are obtained [2]. Depending on the level of detail, the IEEPs may capture the effects of a radome as well as reflections in metallic structures on the platform. The optimization algorithm is identical for optimization using EEPs and IEEPs, and the two approaches only differ based on which dataset is used as input for the optimization. By using IEEPs, it is possible to compensate for the phase shift and reflections in a radome, thereby compensating for the increased sidelobe level often seen when installing the radome [4].

The EEP for antenna element n is denoted by $\vec{f}_n(\hat{r}, \omega) = \hat{n}^{(co)} f_n(\hat{r}, \omega) + \hat{n}^{(cr)} f_n^{(cr)}(\hat{r}, \omega)$, where $f_n(\hat{r}, \omega)$ is the copolarization component at the angular frequency ω. We have used Ludwig's 3rd definition for $\hat{n}^{(co)}$ and $\hat{n}^{(cr)}$ [22] in the implementation. The relation between the electric far-field $\vec{E}_n(\hat{r})$ and the corresponding EEP is [5], [23]

$$\vec{E}_n(\vec{r}, \omega) = \frac{e^{-jkr}}{r} V_n \vec{f}_n(\hat{r}, \omega) \tag{1}$$

where $k = \omega/c$ is the free-space wavenumber. Following [24], it is convenient to choose the following normalization coefficients:

$$V_n = \sqrt{\frac{\eta P_n}{2\pi}} \tag{2}$$

where P_n is the stimulated power at antenna port n used in the simulation or measurement for element n, and η is the free-space impedance.

The copolarization component of the array far-field, evaluated in the unit direction $\hat{r}$, is given by [21]

$$F(\hat{r}, \omega) = \sum_{n=1}^{N} a_n(\omega) f_n(\hat{r}, \omega) \equiv f(\hat{r}, \omega)^T a(\omega). \tag{3}$$

The cross-polarization component is calculated by analogy, by replacing $f_n(\hat{r}, \omega)$ by $f_n^{(cr)}(\hat{r}, \omega)$ in (3). With the notation on the right-hand side of (3), the N excitation coefficients are organized in the frequency-dependent column vector $a(\omega)$. We use the following notation:

$$a_n(\omega) = \alpha_n(\omega) e^{j\Phi_n(\omega)} \tag{4}$$

where α_n and Φ_n are the frequency-dependent real-valued amplitude and phase coefficients, respectively. Note that all EEPs are evaluated in the same system of coordinates. Equation (3) is commonly presented with different phase reference points for each element, whereby an additional exponential factor appears in (3). With the EEPs $\vec{f}_n'(\hat{r}, \omega)$ evaluated in the phase reference point $\vec{r}_n$ of element n, the relation is given by $\vec{f}_n(\hat{r}, \omega) = \vec{f}_n'(\hat{r}, \omega) e^{jk\vec{r}_n \cdot \hat{r}}$, for example, [5].

Here, it is assumed that the relation between a_n in (3) (defined at the antenna port) and the EEP is a good approximation linear. For this to hold, the antenna must not contain any nonlinear material, nonlinear active components, or other sources of nonlinearities. One can also consider an excitation

coefficient a_n' defined at the TRM port. To include the TRM behavior an additional assumption that a_n is linearly dependent on a_n' is needed, which is a good approximation for the receiving case considered in this article.

With the normalization (2), the realized gain is given by [5]

$$G_r(\hat{r}, \omega) = \frac{|\vec{F}(\hat{r}, \omega)|^2}{||a(\omega)||_2^2} \tag{5}$$

where the norm is defined as [25]

$$||a(\omega)||_2^2 \equiv \sum_{n=1}^{N} |a_n(\omega)|^2. \tag{6}$$

The directivity and gain are obtained by analogy by replacing P_n with the radiated or accepted powers, respectively [26]. The partially realized gain is obtained by only including the copolarization component in (5).

B. Constraints on Phase Coefficients Φ_n

The maximum of the array factor will be steered to $\hat{r}_0$ when the frequency-dependent phase shifts

$$\Phi_n(\omega) = -\tau_n \omega \tag{7}$$

are applied, where $\omega = 2\pi f$ is the angular frequency and τ_n are the time delays given by [5]

$$\tau_n = \vec{r}_n \cdot \hat{r}_0/c. \tag{8}$$

A beam squint effect will occur if the frequency dependence does not correspond to (7), which is the case for regular phase shifters, even in the ideal case. Wideband AESAs are, therefore, typically constructed with TTDs, which ideally satisfy (7). In general, a phase-shifting device can be designed to generate a phase shift according to

$$\Phi_n(\omega) = -\tau_n(\omega - \omega_c) + \phi_n^{(c)} \tag{9}$$

where ω_c is an arbitrarily chosen frequency reference point within the bandwidth. In (9), the frequency-dependent term is generated by a TTD, while the frequency-independent term $\phi_n^{(c)} + \tau_n \omega_c$ is generated by a phase shifter. The phase is thus described by the two parameters τ_n and $\phi_n^{(c)}$ for each antenna element.

Based on implementation with (9), the following optimization cases are of interest. The first case is the most general, with τ_n and ϕ_n to be determined from optimization. This corresponds to TRMs implemented with a combination of TTDs and phase shifters. This general optimization problem is, however, not convex since (3) is not a convex function of τ_n. This article will focus on convex optimization, and the nonconvex case will, therefore, not be considered for the simulation results presented here. The following three cases can be solved by convex optimization.

Case A: By taking advantage of (8), τ_n can be considered to be known, while $\phi_n^{(c)}$ is determined from optimization. This formulation will result in the correct scan direction and eliminate beam squint. The corresponding TRMs are implemented with a combination of TTDs and phase shifters. Since optimizing directly for $\phi_n^{(c)}$ does not result in a convex

problem, we instead optimize for the real and imaginary parts of a_n which then turns out as a convex problem. Thereafter, $\phi_n^{(c)}$ is calculated as the angle of a_n in the complex plane. This means that the optimization variables are $\Re(a_n)$ and $\Im(a_n)$ rather than $\phi_n^{(c)}$ and α_n. For further details, see the optimization over complex-valued excitation coefficients in (25).

Case B: The optimization problem with τ_n determined using (8) and $\phi_n^{(c)} = \omega_c = 0$ is a convex problem which corresponds TRMs implemented with TTDs, but with no phase shifters, that is, the most common hardware implementation for wideband AESAs. Since the phase is assumed to be known for this case, this optimization problem is used only to determine optimal amplitude tapering.

Case C: The optimization problem with $\tau_n = 0$ and $\phi_n^{(c)}$ to be determined from optimization is a convex problem (using the trick in Case A) which corresponds to TRMs implemented with phase shifters, but no TTDs, that is, the most common hardware implementation for narrowband AESAs. This means that the phase is set to be a constant function of frequency.

C. Constraints on Amplitude Coefficients α_n

The amplitude coefficients α_n are realized using VGAs. In the same way that a rapidly fluctuating phase is difficult to realize using phase shifters or TTDs, it is difficult to realize an amplification that varies rapidly with frequency. A commonly used relation between gain and frequency for an amplifier within a specified bandwidth is (in decibel scale)

$$\alpha_n^{(dB)}(\omega) = G_{n,\text{center}} + \kappa(\omega - \omega_c) \qquad (10)$$

where $G_{n,\text{center}}$ is the amplitude at the center frequency, at the antenna port of the nth VGA and κ is the gain slope coefficient. By introducing the notation $G_{n,\text{center}} = 20\log_{10}\beta_n$ and $\kappa = 20s$, this is conveniently expressed in linear scale as

$$\alpha_n(\omega) = \beta_n 10^{s(\omega - \omega_c)}. \qquad (11)$$

The gain slope coefficient κ can be either positive or negative depending on the AESA system specification. As an example, a positive gain slope can be used to compensate for losses in long RF cables that have a negative gain slope, thereby resulting in a flat frequency gain on a system level. The same gain slope coefficient is applied to all TRMs, since allowing individual variations would significantly increase the complexity and cost. Hence

$$||a(\omega)||_2^2 = 10^{2s(\omega - \omega_c)}||\beta||_2^2. \qquad (12)$$

By using the normalization $||\beta||_2^2 = 1$ with (2), and inserting (12) into (5), we obtain

$$G_r(\hat{r}, \omega) = \left| \sum_{n=1}^{N} \beta_n e^{j\Phi_n(\omega)} \vec{f}_n(\hat{r}, \omega) \right|^2. \qquad (13)$$

Note that the realized gain (13) is independent of the gain slope coefficient κ. The gain slope coefficient is, therefore, arbitrary and can be specified based on other considerations rather than being determined by the optimization. By comparing (13) to (3), we note that the realized gain can be evaluated as $|\vec{F}(\hat{r}, \omega)|^2$ with

$$\alpha_n(\omega) = \beta_n \qquad (14)$$

that is, an amplitude excitation which is constant in frequency. As demonstrated above, (14) is applicable for calculating the realized gain for an arbitrary gain slope under the assumption that the same gain slope is used for all antenna elements.

III. WIDEBAND OPTIMIZATION ALGORITHM

The optimization program is derived by considering the excitation coefficients a_n as unknown at the reference frequency ω_c, and extending the frequency dependence to the specified bandwidth using (4) with (9) and (14). A phase–frequency relation similar to (9) was used in the optimization program for endfire arrays presented in [12], although the realization with TTDs or phase shifters was not discussed. The optimization program presented below is implemented to optimize the realized gain. The advantage of optimizing the realized gain rather than the directivity is that the mismatch is taken into account in the optimization. This will result in a tradeoff where the total active reflection coefficient (TARC) is taken into account in the optimization implicitly through the realized gain. While the TARC is taken into account implicitly, it can be found using the S matrix introduced in Section II-A.

The array is optimized for a bandwidth BW_{opt}. Meanwhile, the array is used in a bandwidth BW_{uti}, which may be greater than BW_{opt}. The narrowband approach described in the introduction, where a single-frequency optimization is carried out at the center frequency, corresponds to $BW_{\text{opt}} = 0\%$ and $BW_{\text{uti}} > BW_{\text{opt}}$.

Let the bandwidth be sampled at M sample points ω_m

$$\omega_m = \omega_1 + \widetilde{BW}_{\text{opt}} \frac{m - 1}{M}. \qquad (15)$$

In this equation, $\widetilde{BW}_{\text{opt}}$ is the absolute bandwidth expressed in the unit 1 Hz, and BW_{opt} is the corresponding relative bandwidth, described as a percentage. The EEPs are assumed to be known from measurement or simulation at these sample points. By using (4) with (9) and (14), the array gain can be evaluated at all the M frequency samples, with only the N complex-valued $a_n(\omega_c)$ to be determined from optimization. The extension from ω_c to the remaining frequency samples can then be expressed as a matrix multiplication

$$a(\omega) = B(\omega)a(\omega_c) \qquad (16)$$

where $B(\omega)$ is a diagonal $N \times N$ matrix defined by

$$B_{nn}(\omega) = e^{-j(\omega - \omega_c)\tau_n}. \qquad (17)$$

Cases A, B, and C are all implemented with (17). For Case A, τ_n in (17) is determined by (8). For Case C, $B(\omega)$ is an identity matrix since $\tau_n = 0$. Case B is implemented with $\omega_c = 0$.

A. Optimal Sum Pattern With Low Sidelobes, Cases A and C

Similar to [4] and [6], the goal of the optimization method presented here is to minimize the sidelobe level in predefined sidelobe regions. Therefore, the far-field amplitude is sampled at sample points $\hat{r}_i$, $i = 1, 2, \ldots, Q$, in the sidelobe regions Ω, by using the summation (3), that is,

$$F(\hat{r}_i, \omega) = f(\hat{r}_i, \omega)^T B(\omega)a(\omega_c). \qquad (18)$$

The sampled copolarized sidelobe level costs are collected in a vector of length Q

$$s(\omega) = A(\omega)B(\omega)a(\omega_c) \tag{19}$$

where A is a $Q \times N$ complex-valued matrix according to

$$A(\omega) = \begin{pmatrix} p_1(\omega)f(\hat{r}_1, \omega)^T \\ p_2(\omega)f(\hat{r}_2, \omega)^T \\ \vdots \\ p_Q(\omega)f(\hat{r}_Q, \omega)^T \end{pmatrix}. \tag{20}$$

The cross-polarization sidelobe samples are evaluated by analogy by replacing $f(\hat{r}_i, \omega)$ by $f^{(cr)}(\hat{r}_i, \omega)$ in (20). The coefficients p_1, p_2, ..., p_Q are penalty coefficients used to apply varying sidelobe penalties at various regions.

A condition is needed to reject the trivial solution $a = 0$, which would result in a zero sidelobe-level cost. This can be implemented as

$$f(\hat{r}_0, \omega_c)^T a(\omega_c) = 1 \tag{21}$$

which corresponds to unity amplitude and zero phase in the scan direction. The condition (21) is widely used in array antenna optimization, for example, Capton's single-frequency beamformer [27]. In addition to rejecting the trivial solution, (21) can be considered to be a normalization of the vector $a(\omega_c)$ to set the renormalized realized gain in the scan direction to 0 dB at the center frequency. Note that the normalization $||a(\omega)||_2^2 = 1$ used for the realized gain above is a quadratic form, that is, a nonconvex constraint [28]. It is, therefore, practical to use (21) during the optimization, and thereafter renormalize $a(\omega)$ to plot the realized gain. Another advantage with the normalization (21) is that $|f(\hat{r}_i, \omega_c)^T a(\omega_c)|^2$ can be interpreted as the sidelobe level for a direction $\hat{r}_i$ when $\omega = \omega_c$. For $\omega \neq \omega_c$, the situation is slightly different since the sum-pattern gain varies with frequency. One method to take this into account is to consider that the gain scales as $G = 4\pi\epsilon_{\text{eff}}A/\lambda^2 \propto \omega^2$ [5], where A is the aperture area and ϵ_{eff} is the aperture efficiency. We have, therefore, used the following penalty coefficients in the implementation:

$$p_i(\omega) = \omega_c/\omega. \tag{22}$$

It is possible to modify (22) for obtaining a higher sidelobe penalty at the corresponding sample point $\hat{r}_i$, or stricter sidelobe constraints at certain frequencies.

In the next step, we collect the Q sidelobe samples at the M frequencies in a matrix of dimensions $(QM) \times 2$

$$E = (Ca(\omega_c), \ C^{(cr)}a(\omega_c)) \tag{23}$$

where the first column of E contains the copolarized sidelobe-level costs and the second column contains the cross-polarized sidelobe-level costs. The matrices C and $C^{(cr)}$ are of dimension $(QM) \times N$

$$C = \begin{pmatrix} A(\omega_1)B(\omega_1) \\ A(\omega_2)B(\omega_2) \\ \vdots \\ A(\omega_M)B(\omega_M) \end{pmatrix} \tag{24}$$

and $C^{(cr)}$ is defined by analogy. The sidelobe-level cost for each sample can, therefore, be evaluated as the norm of the corresponding row in E.

In conclusion, we have the following convex optimization problem for Cases A and C:

$$\min_{a(\omega_c)\in\mathbb{C}^N} \quad \max \ ||(Ca(\omega_c), \ C^{(cr)}a(\omega_c))||_2$$
$$\text{s. t.} \quad f(\hat{r}_0, \omega_c)^T a(\omega_c) = 1. \tag{25}$$

The norm operation $|| \cdot ||_2$ in (25) is applied to each row in the matrix E, and $\mathbb{C}^N$ is the set of complex-valued vectors of length N. With this formulation, the optimization problem can be directly implemented in a convex optimization tool such as CVX [29]. This optimization problem is used to compute the N unknowns $a(\omega_c)$ which are optimal for the specified bandwidth, BW_{opt}.

In summary, the optimization algorithm needs the following input: First, the N EEPs sampled at M frequencies ω_m in the bandwidth are used as input. The antenna locations $\vec{r}_n$ are also needed as input in the computation of $B(\omega)$. A scan direction $\hat{r}_0$ and sidelobe regions Ω need to be specified. As demonstrated in [4], it is possible to control the shape of the beam to make the beam more narrow or wide depending on the specified sidelobe regions.

B. Optimal Sum Pattern With Low Sidelobes, Case B

Some modification is needed for the optimization program (25) for Case B where only the amplitude coefficients are determined from optimization. This program can be implemented as an optimization over the set of real-valued nonnegative coefficients β. For Case B, $\omega_c = 0$ and (8) are specified in (17). Consider the constraint (21), which is used to reject the trivial solution. With $\phi_n^{(c)} = 0$, (21) is reformulated as $f(\hat{r}_0, \omega_c)^T B(\omega_c)\beta = 1$. This constraint specifies the imaginary part to be zero, which cannot be satisfied, in general, with nonnegative real-valued coefficients β. An alternative constraint is, therefore, used to reject the trivial solution

$$\min \beta \geq \gamma. \tag{26}$$

The parameter $\gamma > 0$ controls the normalization, which can be considered arbitrary since the results will be renormalized to present realized gain. This constraint also differs from (21) in the sense that it prohibits setting any excitation coefficients equal to zero. This is not considered to be a restriction, since setting some coefficients equal to zero would result in a reduced aperture efficiency.

In conclusion, we have the following optimization problem:

$$\min_{\beta\in\mathbb{R}^N} \quad \max \ ||(C\beta, \ C^{(cr)}\beta)||_2$$
$$\text{s. t.} \quad \min \beta \geq 1 \tag{27}$$

where $\mathbb{R}^N$ is the set real numbers in vectors of length N.

C. Optimal Difference Patterns

The monopulse method relies on three simultaneous signals to estimate the DoA: the sum signal, the azimuth difference signal, and the elevation difference signal. The DoA

is estimated from the ratios of difference and sum signals by an estimation algorithm [2], [3]. These three signals are received by the monopulse array in the corresponding sum and difference radiation patterns, referred to using the short-hand notation Σ, Δa, and Δe, respectively. There are multiple array configurations used for obtaining simultaneous sum and difference patterns, for example, [3], [30]. One of the most commonly used subarray configurations is the four-quadrant monopulse array presented in Fig. 2. This section presents a convex optimization program for optimal difference patterns with low sidelobes. Following Section III-A, we will start by considering Cases A and C. A common design of analog feed networks for the four-quadrant monopulse array results in the common excitation weight vector $a(\omega)$ being used for all three patterns Σ, Δa, and Δe. The tradeoff needed to obtain small sidelobes in all three patterns when sharing common excitation weights will be considered in Section III-D.

While sum patterns are computed using (3), difference patterns are computed by

$$F_{\Delta x}(\hat{r}, \omega) = f(\hat{r}, \omega)^T S_x a(\omega) \tag{28}$$

where S_x is a diagonal matrix [4]. The diagonal elements of S_x are either $+1$ or -1, depending on which subarray the corresponding array element belongs to. For the four-quadrant configuration, we use S_a to denote the matrix used for computing the azimuth difference pattern $F_{\Delta a}$, and S_e to denote the matrix used for computing the elevation difference pattern $F_{\Delta e}$. The method presented here is not restricted to the four-quadrant configuration, since any subarray configuration can be considered simply by modifying S_x. The cross-polarization component is computed by analogy by replacing $f(\hat{r}, \omega)$ by $f^{(cr)}(\hat{r}, \omega)$ in (28).

One of the properties of DoA estimation with the monopulse method is that the direction to the target is approximately proportional to the target's displacement from the scan direction $\hat{r}_0$ [2]. Therefore, the difference signal is ideally zero when the target is located in $\hat{r}_0$. To prevent the zero in the difference pattern from drifting away from $\hat{r}_0$ as a result of the chosen excitation, we use the following convex constraint:

$$|f(\hat{r}_0, \omega_m)^T S_x a(\omega_m)| \leq \delta \quad m = 1, \ldots, M \tag{29}$$

where δ is a small tolerance number.

Similar to the optimization of sum patterns described in Section III-B, the difference patterns are also sampled in both polarizations in predefined sidelobe regions by (28). In conclusion, optimal difference patterns for Case A can be computed using the following convex optimization program for Cases A and C:

$$\min_{a(\omega_c) \in \mathbb{C}^N} \quad \max \; ||(C_\Delta a(\omega_c), \; C_\Delta^{(cr)} a(\omega_c))||_2$$
$$\text{s. t.} \; f(\hat{r}_0, \omega_c)^T a(\omega_c) = 1,$$
$$|f(\hat{r}_0, \omega_m)^T S a(\omega_m)| \leq \delta \quad m = 1, \ldots, M \tag{30}$$

where C_Δ is calculated according to (24) with the inclusion of the matrix S_x (i.e., S_e or S_a).

The modification of (30), for Case B follows Section III-B. This modification is presented explicitly in Section III-D for the case of common excitation weights.

D. Monopulse Patterns With Common Excitation Weights

At each frequency sample, there are three specified sidelobe regions: Ω_Σ, $\Omega_{\Delta e}$, and $\Omega_{\Delta a}$ for the sum pattern and the elevation and azimuth difference patterns. Six matrices, that is, C, $C^{(cr)}$, $C_{\Delta e}$, $C_{\Delta e}^{(cr)}$, $C_{\Delta a}$, and $C_{\Delta a}^{(cr)}$, are calculated according to (24) with the inclusion of the matrices S_e and S_a in the evaluation of the difference patterns. As an example, $C_{\Delta e}$ is calculated by (24) with $A(\omega)$ replaced by $A_{\Delta e}(\omega) S_e$, where $A_{\Delta e}$ is sampled in $\Omega_{\Delta e}$. We define D as

$$D = \begin{pmatrix} C \\ l_e C_{\Delta e} \\ l_a C_{\Delta a} \end{pmatrix} \tag{31}$$

with $D^{(cr)}$ calculated analogously. The parameters l_e and l_a are penalty coefficients, which can be used, for example, to allow a larger sidelobe level in the difference patterns compared to the sum pattern. In conclusion, we have the following convex optimization program for Cases A and C:

$$\min_{a(\omega_c) \in \mathbb{C}^N} \quad \max \; ||(Da(\omega_c), \; D^{(cr)} a(\omega_c))||_2$$
$$\text{s. t.} \; f(\hat{r}_0, \omega_c)^T a(\omega_c) = 1$$
$$|f(\hat{r}_0, \omega_m)^T S_a B(\omega_m) a(\omega_c)| \leq \delta, \quad m = 1, \ldots, M$$
$$|f(\hat{r}_0, \omega_m)^T S_e B(\omega_m) a(\omega_c)| \leq \delta, \quad m = 1, \ldots, M. \tag{32}$$

Compared to the optimization problem in Section III-A, this optimization problem contains $2M$ additional constraints, in addition to sidelobe samples also in the difference patterns.

Following Section III-B, (32) can be modified for Case B according to:

$$\min_{\beta \in \mathbb{R}^{+N}} \quad \max \; ||(D\beta, \; D^{(cr)}\beta)||_2$$
$$\text{s. t.} \; \min \beta \geq 1$$
$$|f(\hat{r}_0, \omega_m)^T S_a B(\omega_m) \beta| \leq \delta, \quad m = 1, \ldots, M$$
$$|f(\hat{r}_0, \omega_m)^T S_e B(\omega_m) \beta| \leq \delta, \quad m = 1, \ldots, M. \tag{33}$$

Due to the difference in normalization by using (26) instead of (21), the parameter δ should be set to a larger value in (33) compared to (32).

IV. RESULTS

We first consider a linear array of ideal elements for Case A in Section IV-A. We, thereafter, proceed to investigate a BoR array antenna in Sections IV-B and IV-C, with results for Case A and a comparison to Case B. Lastly, the tradeoff between bandwidth and SLL is investigated in Sections IV-D and IV-E. Section IV-E also shows the usefulness of the method for a more narrowband array.

A. Optimal Wideband Sum Pattern for Ideal Linear Array

Consider a linear array of $N = 40$ idealized elements distributed with an interelement spacing d along the x-axis. The ideal element patterns are modeled in the $\phi = 0°$ cut by

$$f_n(\theta, \omega) = \frac{\sqrt{\pi} d\omega}{\pi c} \frac{\sin\left(\frac{\omega d}{2c} \sin\theta\right)}{\frac{\omega d}{2c} \sin\theta} e^{j(n\omega d/c)\sin\theta}. \tag{34}$$
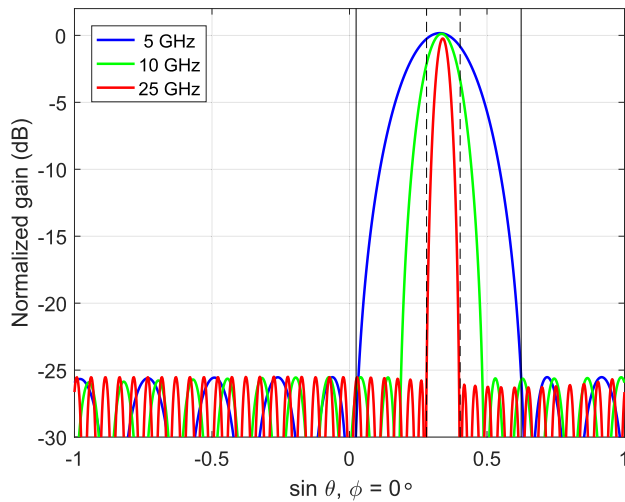
Fig. 3.   Optimal far-field gain for a linear array of $N = 40$ elements, optimized for the bandwidth 5–25 GHz and Case A. The boundaries of the sidelobe regions specified for the optimization are indicated with the vertical lines for 5 GHz (solid) and 25 GHz (dashed). The normalized gain $|(\omega_c/\omega)F|^2$, subject to the normalization constraint (21) is presented, to compare the sidelobe level between the different frequency samples.

Equation (34) is derived from [26] to include the frequency-dependent properties of the antenna elements. As frequency increases, the beamwidth of the ideal element pattern decreases, and the gain increases accordingly. The interelement spacing d was set to $\lambda/2$ at the upper frequency. A 1 : 5 bandwidth from 5 to 25 GHz was used to define BW_{opt} here. The sidelobe regions were specified as $-90° \leq \theta \leq \theta_1$ and $\theta_2 \leq \theta \leq 90°$. Note that the beamwidth scales as $\theta_w = \kappa_w \lambda/(Nd)$ [5], where κ_w is a frequency-independent parameter which depends on the tapering [31]. We, therefore, specify the sidelobe region with $\theta_1 = \theta_0 - \theta_w \omega_c/\omega$ and $\theta_2 = \theta_0 + \theta_w \omega_c/\omega$. A scan angle of $\theta_0 = 20°$ was used. In the presented example, we used $\kappa_w = 1.3$ rad, which results in a sidelobe level better than -25.5 dB for the entire frequency band for Case A. It is a well-known tradeoff that a more narrow beam will result in a higher sidelobe level [5]. The optimal far-field results are presented at 5, 10, and 25 GHz in Fig. 3. The normalized gain $|F(\theta, \omega)(\omega_c/\omega)|^2$, subject to the normalization constraint (21), is presented, to compare the sidelobe level between the different frequency samples. As expected, there is no notable beam squint in the figure. Furthermore, the normalized maximum gain is close to 0 dB for all frequency samples, indicating that the gain is increasing with frequency proportionally to ω^2, which is expected based on the discussion above. This demonstrates that this optimization method can be used to obtain low sidelobes over a very large bandwidth. It is interesting to note that for ideal antenna elements, increasing the bandwidth does not seem to result in a tradeoff with respect to sidelobe level.

B. Optimal Wideband Sum Pattern for Airborne EW Array

The body of revolution (BoR) array [32] illustrated in Fig. 2 and partially in Fig. 4 is an array antenna type which is well suited for airborne EW. For a single-polarized array, the BoR array can be considered similar to a tapered slot array [33],
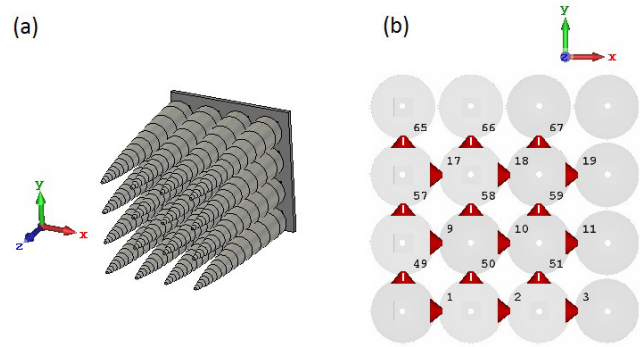

Fig. 4.   (a) Dual-polarized BoR array of 4×4 BoR elements. (b) Discrete ports for feeding 3×3 horizontal antenna elements (solid red, numbering 1–19) and discrete ports for feeding 3×3 vertical antenna elements (red with white stripe, numbering 49–67). Note that the dual-polarized BoR array is not symmetrical. The antenna element numbering corresponds to an array of 6×8 antenna elements for each polarization, as used for the simulation results.

[34]. For dual-polarization, on the other hand, the BoR array has some mechanical and fabrication advantages compared to the dual-polarized Vivaldi array, as described in [32]. Note that the dual-polarized BoR array antenna has asymmetrical edges, as illustrated in Fig. 4. The considered BoR array prototype has $N_x = 8$ columns along the x-axis and $N_y = 6$ rows along the y-axis. This array, therefore, consists of a total of 96 antenna elements, with $N = N_x N_y = 48$ elements per polarization. We consider an implementation with switches between the two polarization modes, and we, therefore, only consider one polarization at a time for the optimization. While we only use 48 elements at a time, it is interesting to note that it is in principle possible to compensate for the cross-polarization of the array by using all 96 elements. Compensation of cross-polarization using the information in the EEPs can be relevant for achieving deep nulls for interference nulling [35]. With only 48 elements used at a time, this is a relatively small array antenna with a wide beamwidth, particularly at the lower frequencies. Being this small, there are also quite significant mutual coupling effects due to the edge truncation.

The unit cell dimension of 6 mm was chosen as half wavelength of the upper frequency 25 GHz. The unit cell was optimized for minimizing the active reflection coefficient in the frequency band 10–25 GHz, by frequency-domain unit cell analysis in CST Microwave Studio. Thereafter, the EEPs for the finite array were computed using the finite integration technique (FIT) implemented in CST Microwave Studio.

The example of a sum pattern presented in Fig. 5 was computed with a scan direction of $\theta_0 = 20°$, $\phi = 0°$, for the specified bandwidth 10–25 GHz and Case A. Similar to Section IV-A, the sidelobe regions used for the optimization were frequency-dependent to allow the beam to widen toward the lower frequencies. The first null of the pattern for uniform amplitude excitation, with a progressive phase shift to steer the main beam to the desired scan angle, was used when specifying the sidelobe regions. Therefore, the optimal far-field pattern has a null–null beamwidth which is comparable to that of a uniformly excited array. To obtain a low sidelobe level,
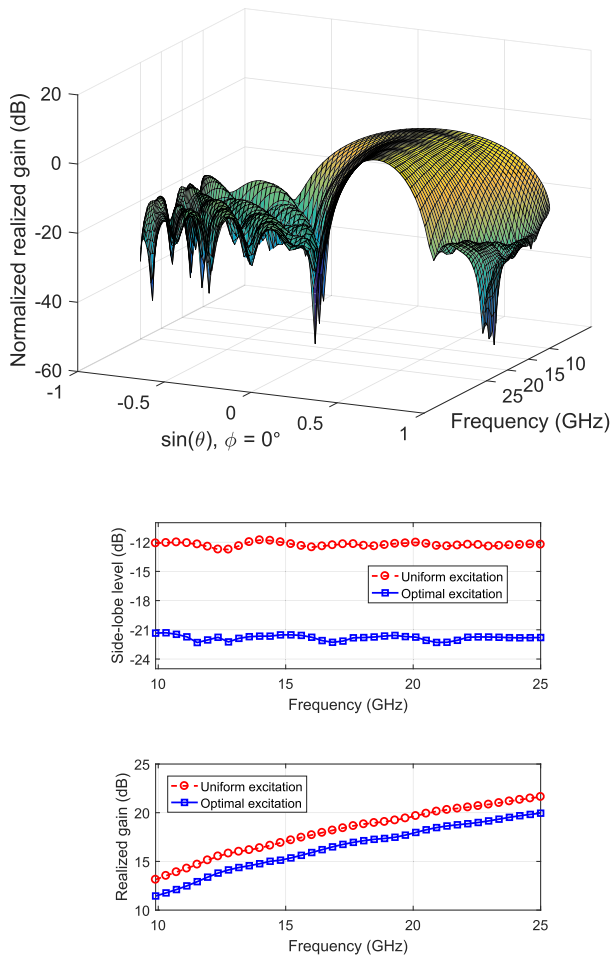
Fig. 5. (a) Optimal sum pattern for the BoR array scanned to $\theta_0 = 20°$, optimized for the bandwidth 10–25 GHz and Case A. The realized gain, renormalized according to $|(\omega_c/\omega)\bar{F}|^2$ subject to (21), is presented to compare the sidelobe level between the different frequency samples. (b) Sidelobe level as a function of frequency. (c) Realized gain as a function of frequency, showing the aperture efficiency compared to a uniformly excited array.
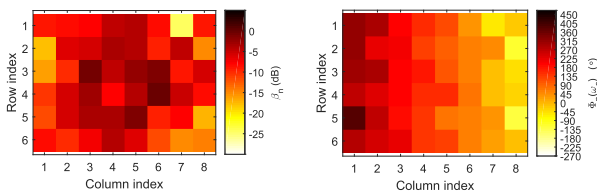

Fig. 6. Optimal excitation coefficients corresponding to Fig. 5 evaluated at the reference frequency point ω_c in both amplitude (left) and phase (right). The phase is close to the progressive phase shift expected for steering the main beam to $\theta_0 = 20°$, $\phi_0 = 0°$.

it is necessary to modify the sidelobe regions to allow the beam to widen further, due to the well-known tradeoff between sidelobe level and beamwidth.

There is no notable beam squint shown in Fig. 5(a). The sidelobe level shown in Fig. 5(b) is better than -21 dB for all frequency samples in the band. It is well known that tapering used to reduce the sidelobe level will also contribute to widening the beam and lowering the gain [5]. The difference in the gain compared to a uniformly excited array is typically presented as a gain reduction (in decibels) or an aperture

efficiency (in percentage). As shown in Fig. 5(c), the gain reduction is smaller than 1.8 dB within the bandwidth.

The optimal amplitude and phase excitation coefficients for this example are shown in Fig. 6. First, it is interesting to note the optimal phase is close to the ideal progressive phase shift which is required for steering the beam to $\hat{r}_0$. The amplitude tapering has some tapering toward the array edges, as usually seen for low sidelobes. Since the array antenna is small with significant mutual coupling effects, the optimal amplitude excitation varies rapidly from element to element [see Fig. 6(a)]. Furthermore, since the array is subject to asymmetrical edges, as illustrated in Fig. 4, we do not expect the optimal amplitude excitation to be symmetrical.

Fig. 5 was computed for Case A. It is interesting that the sidelobe level obtained for Case B, which uses only TTDs and not phase shifters is 1.53 dB higher. This indicates that some performance improvement can be achieved by combining phase shifters and TTDs, compared to only using TTDs.

C. Optimal Wideband Monopulse Patterns With Common Excitation Weights

The BoR array far-field data described in the previous section was used for computation of optimal monopulse excitation, using the convex optimization program (32). The same sidelobe regions and scan direction described in Section IV-B were used for the sum pattern with a beam widening factor of 10%. The beam widening factor is introduced due to the observation that the tradeoff required for low sidelobes with common excitation weights requires some beam widening to achieve low sidelobe levels. The sidelobe regions for the difference patterns were determined from the sum pattern sidelobe regions, with a 20% increase in width compared to the sum pattern. The optimization parameters $\delta = 10^{-2}$, $l_e = l_a = 1$ [see (31) and (32)] were used, giving the same penalty for sidelobes in the sum pattern or either of the difference patterns. The optimal far-field patterns are shown in Fig. 7 for a number of frequency samples within a 4.9-GHz bandwidth, defining BW_{opt} as in (15). The maximum sidelobe level occurring within the bandwidth in all three patterns is -18.6 dB. Similar to the sum pattern example in Section IV-B, there is no notable beam squint. Furthermore, a sharp null is produced in the difference patterns. Due to the absence of beam squint, the null is not moving when sweeping the frequency. The maximum sum pattern gain reduction in the band is 1.95 dB compared to a uniform excitation.

Interestingly, the optimal excitation for Case B as computed by the optimization problem (33) is similar to the uniform excitation. The maximum sidelobe level within the 4.9-GHz bandwidth for the optimal excitation with (33) is -12.4 dB, whereas the sidelobe level for uniform excitation is -10.8 dB. These results indicate that the phase variation plays an important role in minimizing sidelobe levels for common excitation weights.

D. Tradeoff Between the Sidelobe Level and Bandwidth for a Wideband Monopulse Array

It is a common practice to use switched or tunable filters to adjust the instantaneous bandwidth to a specific band to
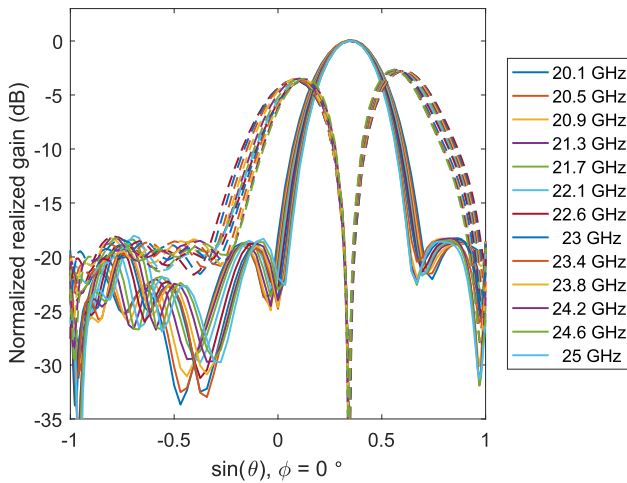
Fig. 7. Sum pattern (solid) and corresponding difference pattern (dashed), steered to $\theta_0 = 20°$. The renormalized gain $|(\omega_c/\omega)\vec{F}|^2$, subject to the normalization constraint (21) is presented, to compare the sidelobe level between the different frequency samples.

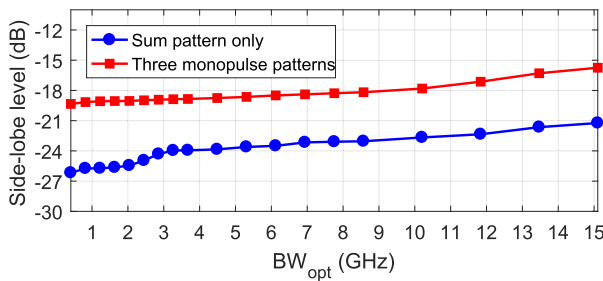Fig. 8. Tradeoff relation between the maximum sidelobe level and BW_{opt}. Simulation results for a BoR array of 6×8 elements, for the scan direction $\theta_0 = 20°$, $\phi = 0°$, optimized for Case A.

reduce the noise level and to filter unwanted signals, for example, [36]. In this section, we investigate the relation between optimal sidelobe level and instantaneous bandwidth for the monopulse array in Fig. 2 by varying BW_{opt}.

The relation between BW_{opt} and maximum sidelobe level is shown in Fig. 8. That is, $BW_{opt} = BW_{uti}$ in Fig. 8, which was computed with the upper frequency 25 GHz fixed, and sweeping the lower frequency. As described in Sections IV-A–IV-C, the sidelobe regions used for optimization are frequency-dependent to allow the beam to widen at the lower frequencies. If the same sidelobe regions had been used for all frequency samples, then the slope in Fig. 8 would be more significant, since this would force a more narrow beam and thus higher sidelobe levels at the lower frequencies. By allowing the beam to widen as the frequency is decreased, the slope in Fig. 8 is instead determined by other factors, as described below.

For realistic (i.e.,, nonideal) antennas, it is expected that the sidelobe level will increase as BW_{opt} increases, even if this is not caused by the beamwidth described above. This is due to the sample matrices C and D containing additional frequency information, which directly affects the tradeoff determined by optimization. This optimization formulation allows the excitation to compensate for some nonideal properties of the EEPs, and this will be more challenging the larger BW_{opt} is.
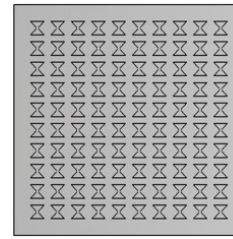

Fig. 9. 10×10 bowtie array that is used for the narrowband investigation. At the center frequency, the elements are $1/3\lambda \times 1/3\lambda$ and spaced 0.5λ apart, center to center. The elements lie 0.27λ over a ground plane, which extends out 0.42λ past the edge elements.

Based on the above, the slope in Fig. 8 can be attributed to the nonideal properties of the EEPs in relation to the constraints on the frequency variation of the excitation coefficients.

The monopulse optimization with common excitation weights finds a tradeoff for simultaneously small sidelobes in three patterns (i.e., Σ, Δ_e, and Δ_a). It is, therefore, expected that the sidelobe level will be higher for monopulse excitation with common excitation weights compared to only the sum pattern.

E. Tradeoff Between the Sidelobe Level and Bandwidth for a Narrowband Array

Although the optimization method was developed for wideband arrays, we here illustrate the method's behavior and applicability to a comparatively more narrowband array. We will here investigate cases where BW_{opt} ranges from 0% to 30%, varying symmetrically around the center frequency, for a bowtie array designed for $BW_{uti} = 30\%$ shown in shown in Fig. 9. The optimization is run for Case A, for example, optimization problem (25) with a far-field sampling of $2°$ in both azimuth and elevation. The far-field sampling is increased to $0.5°$ at the border between the mainlobe and the sidelobe region.

The same definition for the sidelobe region as in Section IV-B was used for this investigation. The beamwidth of an array with uniform excitation scales with frequency. It is important that the angular sampling is fine enough to capture this scaling to obtain a low sidelobe-level growth.

The resulting maximum SLL within BW_{uti} is shown in Fig. 10. Each trace represents one optimization bandwidth BW_{opt} with a varying BW_{uti}. The point at which BW_{uti} becomes larger than BW_{opt} is highlighted by a circle. It is clear that the SLL degrades as $BW_{uti} > BW_{opt}$, which is shown in a rapid increase in this outer region, as indicated by dashed lines. Consider, for example, the single-frequency optimization, that is, $BW_{opt} = 0\%$, which achieves -28.1 dB SLL. If $BW_{uti} = 5\%$, the 0% optimization instead gives an SLL of -24.1 dB.

Similar to the results in Fig. 8, Fig. 10 shows an increase in SLL with increasing BW_{opt}. It can also be seen that as long as BW_{uti} is smaller than BW_{opt} (solid-colored lines), maximum SLL is essentially constant.

Compared to the single-frequency example, running the optimization over the full 5% instead gives -26.9 dB SLL over BW_{uti}. Thus, optimizing for the desired BW_{uti} improves

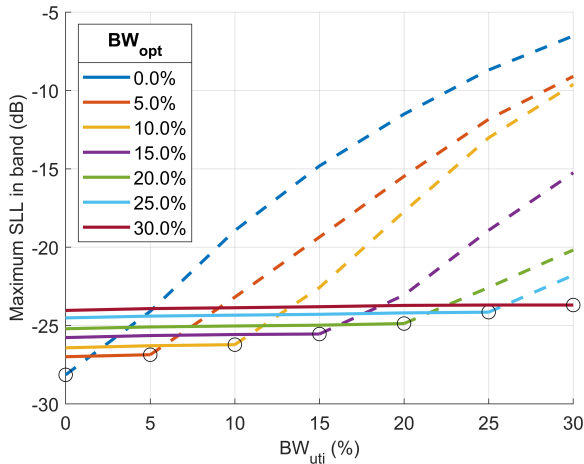Fig. 10. Peak sidelobe level within a utilized bandwidth BW_{uti}. Plotted for a set of optimization bandwidths BW_{opt}. The edge of the optimization bandwidth is highlighted by a circle, with the realized SLL for bandwidths outside BW_{opt} marked with a dashed line. Simulation results for a 10×10 bowtie array, for the scan direction $\theta_0 = 30°$, $\phi = 0°$, optimized for Case A. .

the SLL by 2.8 dB. Similar improvements can be seen for all combinations of BW_{uti} and BW_{opt}. Another observation from Fig. 10 is that any increase in BW_{opt}, up until it reaches BW_{uti}, lowers the maximum SLL in BW_{uti}.

Note that optimizing over a bandwidth comes with an increased computational cost, both in terms of storing more far-field data and in time. For a single frequency, the single-frequency optimization takes 95 s compared to 550 s for the 5% bandwidth. These timings were obtained using an Intel Xeon Gold 5217 with 192 GB RAM. This hardware is not a requirement for the program, and some of the results presented here were computed using a regular laptop with 16 GB RAM.

V. DISCUSSION AND CONCLUSION

This article presents a convex optimization program applied to wideband EW AESAs. The optimization is carried out for a specified bandwidth rather than a single frequency. This eliminates the degradation in performance close to the band edges typically found when a single-frequency optimization is used at the center frequency. This applies to degraded performance caused by using an optimization that is only optimal at the center frequency, and suboptimal at the band edges as seen in Fig. 10. Degradation can also occur at the band edges due to the limited bandwidth of the antenna elements and the radome. The convex optimization program presented here will find a tradeoff to compensate for these effects based on the EEPs data, to obtain the best performance for the specified bandwidth. Thanks to the implementation in terms of EEPs, the effects of mutual coupling and installation (e.g., radome effects [4]) can be compensated for, to some extent, using the optimization program. This introduction of wideband optimization is a significant improvement to the narrowband, single-frequency optimization program in [4].

The presented method has been developed for EW arrays of moderate size. With $M = 50$, $N = 48$, and using a far-field

sample spacing of $0.5°$ in both azimuth and elevation, the EEP dataset is 50 GB. This demonstrates that the size of the problem is moderate for small-array antennas, but the size of the problem is growing as the number of antenna elements or the number of frequency samples increases. For a radar array with $M = 15$ and $N = 1000$, 313 GB of EEP data would be needed. While possible to optimize, the simulations required to find the EEPs would be inefficient using a full wave solver. EW arrays can be small compared to radar arrays as a wider lobe is desired for a higher probability of intercept [37]. Based on the above, the method presented is deemed to be mainly useful for small- and mid-sized array antennas, such as those used in EW and communications. Approximations may be needed to efficiently model very large-array antennas used in, for example, some radar applications.

The presented convex optimization program fixes the variation of both amplitude and phase coefficients with frequency to a predefined function. The rapid phase variations typically seen when carrying out a single-frequency optimization at every frequency sample in the bandwidth [12] are, therefore, eliminated. The predefined functions are directly compatible with the typical AESA construction shown in Fig. 1(a). Furthermore, the amplitude coefficients can have an arbitrary gain slope, but the same gain slope is used for each TRM. As demonstrated above, the gain slope coefficient does not influence the array realized gain pattern, and it can, therefore, be chosen freely based on other considerations.

It should be noted that the TRM model is assumed to be linear, that is, all components operate within the linear power region. While this may be sufficient for some applications, nonlinearities may be unavoidable in others. These nonlinearities will perturb the optimal solution and cause undesired effects, such as a higher SLL or lower gain [14]. Overtones due to stimulation in the lower part of the frequency band may be radiated if the bandwidth is sufficiently large. These undesired effects could cause sidelobes which are not modeled in this article, as this article mainly focuses on an EW array receiving weak signals.

Constraints were introduced on the frequency variation of the amplitude and phase coefficients, to make it possible to determine realizable, optimized excitation coefficients in an AESA. The numerical results indicate that this optimization program performs well in determining optimal wideband excitation for low sidelobe levels. The implementation with TTDs prevents beam squint, which is demonstrated in the presented results. It was shown that there is a tradeoff relation where the sidelobe level increases as the instantaneous bandwidth is increased.

There are three implementation variations of interest for the presented program, referred to as Case A, Case B, and Case C, respectively. Numerical results are not presented here for Case C, since we are mainly interested in wideband EW arrays where the beam squint inherent in using phase shifters instead of TTDs is not acceptable. That being said, we expect that Case C will be a useful tool for arrays of a smaller bandwidth, particularly for certain radar and communication arrays. A more narrowband system also benefits from this wideband

optimization approach, which eliminates the degradation of SLL at the band edges. Even at a 5% bandwidth, significant improvements to SLL are shown.

In addition to Cases A, B and C, the presented program can be implemented for various types of patterns. We have presented the implementation for optimal sum patterns with small sidelobes, in addition to the implementation for optimal difference patterns with low sidelobes. Furthermore, the implementation of common excitation weights is used to compute the optimal tradeoff which results in low sidelobes in one sum pattern and two difference patterns, which all share common excitation weights. An interesting observation is that Case B applied to common excitation weights results in an amplitude tapering close to the uniform excitation. These results indicate that the optimal phase variation plays an important role in the low sidelobe levels obtained for common excitation weights with Case A.

The presented convex program assumes that the time delays are known from (8). This approach enables the problem to be solved by a convex program and results in good performance for wide and narrow bandwidths. For future work, it is of interest to investigate if the performance can be increased further by using the general, nonconvex method, where time delays are also determined from optimization.

ACKNOWLEDGMENT

REFERENCES

[1] A. De Martino, *Introduction To Modern EW Systems*. Norwood, MA, USA: Artech House, 2012.

[2] H. Frid, J. Malmström, and B. L. G. Jonsson, "Determining direction-of-arrival accuracy for installed antennas by postprocessing of far-field data," *Radio Sci.*, vol. 54, no. 12, pp. 1204–1221, Dec. 2019.

[3] U. Nickel, "Overview of generalized monopulse estimation," *IEEE Aerosp. Electron. Syst. Mag.*, vol. 21, no. 6, pp. 27–56, Jun. 2006.

[4] H. Frid and B. L. G. Jonsson, "Compensation of radome effects in small airborne monopulse arrays by convex optimization," in *Proc. 12th Eur. Conf. Antennas Propag. (EuCAP)*, Apr. 2018, pp. 1–5.

[5] R. J. Mailloux, *Phased Array Antenna Handbook*, vol. 2. Norwood, MA, USA: Artech House, 2005.

[6] H. Lebret and S. Boyd, "Antenna array pattern synthesis via convex optimization," *IEEE Trans. Signal Process.*, vol. 45, no. 3, pp. 526–532, Mar. 1997.

[7] C. Bencivenni, M. V. Ivashina, R. Maaskant, and J. Wettergren, "Design of maximally sparse antenna arrays in the presence of mutual coupling," *IEEE Antennas Wireless Propag. Lett.*, vol. 14, pp. 159–162, 2015.

[8] G. Gottardi, L. Poli, P. Rocca, A. Montanari, A. Aprile, and A. Massa, "Optimal monopulse beamforming for side-looking airborne radars," *IEEE Antennas Wireless Propag. Lett.*, vol. 16, pp. 1221–1224, 2017.

[9] S. Kwak, J. Chun, D. Park, Y. K. Ko, and B. L. Cho, "Asymmetric sum and difference beam pattern synthesis with a common weight vector," *IEEE Antennas Wireless Propag. Lett.*, vol. 15, pp. 1622–1625, 2016.

[10] A. F. Morabito and P. Rocca, "Optimal synthesis of sum and difference patterns with arbitrary sidelobes subject to common excitations constraints," *IEEE Antennas Wireless Propag. Lett.*, vol. 9, pp. 623–626, 2010.

[11] B. Fuchs, "Application of convex relaxation to array synthesis problems," *IEEE Trans. Antennas Propag.*, vol. 62, no. 2, pp. 634–640, Feb. 2014.

[12] J. Helander, D. Tayli, and D. Sjöberg, "Synthesis of large endfire antenna arrays using convex optimization," *IEEE Trans. Antennas Propag.*, vol. 66, no. 2, pp. 712–720, Feb. 2018.

[13] M. Gavell, S. E. Gunnarsson, I. Angelov, Z. S. He, M. Ferndahl, and H. Zirath, "Design and analysis of a wideband Gilbert cell VGA in 0.25-μm InP DHBT technology with DC-40-GHz frequency response," *IEEE Trans. Microwave Theory Techn.*, vol. 65, no. 10, pp. 3962–3974, Oct. 2017.

[14] R. L. Haupt, "Active electronically scanned array technology," in *Timed Arrays: Wideband and Time Varying Antenna Arrays*. Hoboken, NJ, USA: Wiley, 2015, ch. 6, pp. 95–125.

[15] D. P. Scholink and J. O. Coleman, "Formulating wideband array-pattern optimizations," in *Proc. IEEE Int. Conf. Phased Array Syst. Technol.*, May 2000, pp. 489–492.

[16] D. P. Scholnik and J. O. Coleman, "Optimal design of wideband array patterns," in *Proc. Rec. IEEE Int. Radar Conf.*, May 2000, pp. 172–177.

[17] W. Liu and S. Weiss, *Wideband Beamforming: Concepts Technology*, vol. 17. Hoboken, NJ, USA: Wiley, 2010.

[18] L. Feng, G. Cui, X. Yu, R. Liu, and Q. Lu, "Wideband frequency-invariant beamforming with dynamic range ratio constraints," *Signal Process.*, vol. 181, Apr. 2021, Art. no. 107908.

[19] S. Yan, Y. Ma, and C. Hou, "Optimal array pattern synthesis for broadband arrays," *J. Acoust. Soc. Amer.*, vol. 122, no. 5, pp. 2686–2696, Nov. 2007.

[20] L. Chen, Y. Liu, S. Yang, and Y. J. Guo, "Efficient synthesis of filter-and-sum array with scanned wideband frequency-invariant beam pattern and space-frequency notching," *IEEE Signal Process. Lett.*, vol. 28, pp. 384–388, 2021.

[21] D. M. Pozar, "The active element pattern," *IEEE Trans. Antennas Propag.*, vol. 42, no. 8, pp. 1176–1178, Apr. 1994.

[22] A. Ludwig, "The definition of cross polarization," *IEEE Trans. Antennas Propag.*, vol. AP-21, no. 1, pp. 116–119, Jan. 1973.

[23] A. K. Bhattacharyya, *Phased Array Antennas: Floquet Analysis, Synthesis, BFNs and Active Array Systems*, vol. 179. Hoboken, NJ, USA: Wiley, 2006.

[24] H. Frid, H. Holter, and B. L. G. Jonsson, "An approximate method for calculating the near-field mutual coupling between line-of-sight antennas on vehicles," *IEEE Trans. Antennas Propag.*, vol. 63, no. 9, pp. 4132–4138, Sep. 2015.

[25] A. W. Naylor and G. R. Sell, *Linear Operator Theory in Engineering and Science*. Cham, Switzerland: Springer, 2000.

[26] C. A. Balanis, *Antenna Theory: Analysis and Design*. Hoboken, NJ, USA: Wiley, 2016.

[27] H. Krim and M. Viberg, "Two decades of array signal processing research: The parametric approach," *IEEE Signal Process. Mag.*, vol. 13, no. 4, pp. 67–94, Jul. 1996.

[28] S. Boyd and L. Vandenberghe, *Convex Optimization*. Cambridge, U.K.: Cambridge Univ. Press, 2004.

[29] *CVX: MATLAB Software for Disciplined Convex Programming*, Version 2.0, CVX Res., Austin, TX, USA, Aug. 2012. [Online]. Available: https://cvxr.com/cvx

[30] P. Lopez, J. A. Rodriguez, F. Ares, and E. Moreno, "Subarray weighting for the difference patterns of monopulse antennas: Joint optimization of subarray configurations and weights," *IEEE Trans. Antennas Propag.*, vol. 49, no. 11, pp. 1606–1608, Nov. 2001.

[31] H. Frid, "Closed-form relation between the scan angle and feed position for extended hemispherical lenses based on ray tracing," *IEEE Antennas Wireless Propag. Lett.*, vol. 15, pp. 1963–1966, 2016.

[32] H. Holter, "Dual-polarized broadband array antenna with BOR-elements, mechanical design and measurements," *IEEE Trans. Antennas Propag.*, vol. 55, no. 2, pp. 305–312, Feb. 2007.

[33] H. Holter, T.-H. Chio, and D. H. Schaubert, "Experimental results of 144-element dual-polarized endfire tapered-slot phased arrays," *IEEE Trans. Antennas Propag.*, vol. 48, no. 11, pp. 1707–1718, Nov. 2000.

[34] D. H. Schaubert and T. Chio, "Perspectives on radio astronomy: Technologies for large antenna arrays," in *Proc. Conf. ASTRON*, A. B. Smolders and M. P. Haarlem, Eds. Institute in Dwingeloo, Apr. 1999, p. 354.

[35] H. Bui-Van, V. Hamaide, C. Craeye, F. Glineur, and E. de Lera Acedo, "Direct deterministic nulling techniques for large random arrays including mutual coupling," *IEEE Trans. Antennas Propag.*, vol. 66, no. 11, pp. 5869–5878, Nov. 2018.

[36] P. H. Young, *Electronic Communication Techniques*. New York, NY, USA: Merrill, 1994.

[37] H. Frid, "Analysis and optimization of installed antenna performance," Ph.D. dissertation, Dept. EECS, Kungliga Tekniska Ḧgskolan, Stockholm, Sweden, 2020.

[38] "Method for operating wide-band AESA," WO Patent 2 023 055 262 A1, Apr. 06, 2023.

Henrik Frid received the M.Sc. degree in engineering physics and the Ph.D. degree in electrical engineering from the KTH Royal Institute of Technology, Stockholm, Sweden, in 2015 and 2020, respectively.

From 2018 to 2023, he worked in project management and team-leading roles at Saab, Järfälla, Sweden, where he is currently the Head of Development Pipeline, Naval Software, which is part of Saab Surveillance. His Ph.D. project was carried out partly at Saab, where he worked with computational electromagnetics for antennas installed on aircraft. He has been involved in multiple research projects spanning topics from antenna technology, array antennas, lenses, radomes, geometric optics, electronic warfare, radar, and electromagnetic theory, to dielectric breakdown in liquid high-voltage insulators, RF-MEMS switches, and MEMS for THz applications. He is the inventor of two patents and the author of more than 20 scientific publications, of which seven papers have been published in international peer-reviewed journals, with the remaining papers being published in peer-reviewed conferences. In addition to these technical interests, he also takes an interest in communication and leadership.

Dr. Frid received the 2012 Multiphysics Student Award, he was selected for the 2014 Excellence Doctoral Program at the KTH, and the URSI Young Scientist Award at the 2018 AT-RASC conference.

Harald Hultin received the M.Sc. degree in electrical engineering from the KTH Royal Institute of Technology, Stockholm, Sweden, in 2019. He is currently pursuing the Ph.D. degree with Saab, Järfälla, Sweden, and the KTH Royal Institute of Technology.

He worked as an RF engineer in computational electromagnetics, antenna design, and microwave technology at Saab. His research interests include efficient computational methods, antennas, and electromagnetic theory, in general.

B. L. G. Jonsson received the M.Sc. degree in engineering physics from Umeå University, Umeå, Sweden, in 1995, and the Ph.D. degree in electromagnetic theory from the KTH Royal Institute of Technology, Stockholm, Sweden, in 2001.

He was a Post-Doctoral Fellow at the University of Toronto, Toronto, ON, Canada, until 2004, and a Wissenschaftlicher Mitarbeiter at ETH Zürich, Zürich, Switzerland, until 2006. In 2006, he was with the Electromagnetic Engineering Laboratory, KTH Royal Institute of Technology, where he was an Assistant Professor. He was appointed as a Docent in electromagnetic theory and he became an Associate Professor in 2006. Since 2015, he has been a Professor with the School of Electrical Engineering and Computer Science, KTH Royal Institute of Technology. He leads a Research Group that works with electromagnetic applications, mainly antennas, and arrays antennas. His current research interests include electromagnetic theory in a wide sense.